



Research Paper

Energy-confined solar thermal ammonia synthesis with K/Ru/TiO_{2-x}H_x

Chengliang Mao, Linghao Yu, Jie Li, Jincai Zhao, Lizhi Zhang*



Key Laboratory of Pesticide & Chemical Biology of Ministry of Education, Institute of Environmental & Applied Chemistry, College of Chemistry, Central China Normal University, Wuhan 430079, PR China

ARTICLE INFO

Keywords:

Solar thermal catalysis
Photocatalysis
Ammonia synthesis
Disordered titanium oxide
Incorporated hydrogen
Oxygen vacancies
LSPR

ABSTRACT

Haber–Bosch thermal ammonia synthesis is of energy-intensive nature. Using solar energy for ammonia synthesis is idealized for both energy and environment problems, but remains great challenges. Generally, the diffuse solar flux and inefficient utilization cannot meet the energy demand for NH₃ production. Here we develop a solar thermal avenue, realizing highly efficient solar ammonia synthesis over K/Ru/TiO_{2-x}H_x. The supported Ru is efficient for nitrogen activation because of the electron donation from TiO_{2-x}H_x and free from H₂ poisoning, because the interfacial TiO_{2-x}H_x accepts H atoms from Ru and then delivers them to the Ru activated N₂ to form Ti-NH_x ($x = 1\text{--}3$) even at room temperature. When only irradiated with sunlight, this catalyst absorbs sunlight in the whole UV–vis–NIR region and reaches 360 °C by its plasmonic behavior, exhibiting a Haber–Bosch thermocatalysis-comparable NH₃ generation rate. This solar thermal approach with K/Ru/TiO_{2-x}H_x provides a promising renewable way for ammonia synthesis.

1. Introduction

Haber–Bosch ammonia synthesis lays the foundation for all nitrogen containing chemicals production, being of vital importance to nitrogen chemistry [1,2]. Industrially, the reduction of N₂ with H₂ to give NH₃ relies on Fe-based or Ru-based thermal catalysis. The catalysis process obeys Langmuir–Hinshelwood mechanism, where reactants are first dissociatively adsorbed on the catalyst surface with successive recombination steps [3,4]. Nitrogen activation (dissociative adsorption) is the rate-limiting step for the huge bond energy (945 kJ mol⁻¹) of N≡N [4]. Adsorbed NH_x ($x = 0, 1, 2$) destabilization is also a key step to avoid the catalyst surface blocking because of strong adsorption [4,5]. Both nitrogen activation and NH_x destabilization are high energy demanding, therefore severe temperature and pressure (300–600 °C, 150–250 atm) are required for industrial ammonia synthesis. The energy input stemmed largely from fossil fuel, which has arisen intertwined energy and environment concerns. Using solar energy to drive ammonia synthesis is therefore of great interest because solar irradiation is a promising and renewable alternate for fossil fuel. However, the low energy density of diffuse solar flux challenges solar utilization.

Localized surface plasmon resonance (LSPR) effects of nanostructures are potential for solar ammonia synthesis. They are known to concentrate the diffuse solar flux to generate electromagnetic field (MF) and heat in small volume [6]. Such an LSPR effect is efficient for solar utilization. Also, the plasmonic near-field or localized heating might generate energetic electrons to overcome the high energy barriers

within ammonia synthesis. Ru is a plasmonic metal capable of absorbing sunlight in the whole UV–vis–NIR region (200–2500 nm) and also the conventional catalyst for ammonia synthesis [7–9], thus it becomes a perfect bridge for both efficient solar utilization and ammonia synthesis. Although Ru is not efficient to generate LSPR, its LSPR can be enhanced by coupling with supports of abundant localized electronic states [10], probably because such supports (for example, MoO_{3-x} and WO_{3-x}) have strong LSPRs and thus to facilitate the LSPR of Ru via plasmon hybridization effect [11–13]. Moreover, such supports may simultaneously act as light absorber for efficient solar utilization [11–14], and “electronic promoter” for accelerated N₂ activation in ammonia synthesis, whose excess electrons on the localized electronic states may donate to Ru. If the final H₂ poisoning problem can be solved for electronically promoted Ru, originating from strongly adsorbed H atoms to inhibit the efficient dissociative adsorption of N₂ on the Ru surface [9,15], the dream of using solar energy for efficient ammonia synthesis will come true.

Herein we demonstrate that a solar thermal catalysis strategy with a K promoted, TiO_{2-x}H_x supported Ru catalyst (K/Ru/TiO_{2-x}H_x) could realize the efficient ammonia synthesis without any extra thermal energy under atmospheric pressure. Within this catalyst, both K and the electron-rich support TiO_{2-x}H_x of abundant oxygen vacancies (V_Os) can tune electronic structure of Ru for the efficient nitrogen activation, and the reversibly incorporated H atoms (H_{inc}) in TiO_{2-x}H_x well suppress the H₂ poisoning of electronically promoted Ru. The catalyst absorbs sunlight in the whole UV–vis–NIR region, then converts sunlight into heat

* Corresponding author.

E-mail address: zhanglz@mail.ccnu.edu.cn (L. Zhang).

to meet the temperature requirement for the catalytic ammonia synthesis, and also MF to accelerate the electron transfer during the whole catalytic process. Therefore, the Haber-Bosch thermal catalysis comparable reactivity can be achieved with only sunlight irradiation on the catalyst.

2. Experimental

2.1. Sample preparation

2.1.1. K/Ru/TiO_{2-x}H_x

TiO_{2-x}H_x was prepared from crystalline TiO₂ (Degussa P25) by a solid NaBH₄ reduction and fast cooling method, a modified method from previous protocols [16]. First, 1 g of TiO₂ was mixed with 2 g of NaBH₄ and thoroughly grounded under infrared lamp. The mixture of NaBH₄ and TiO₂ was transferred into a crucible with cap under Ar purging, heated to 380 °C and maintained for 1 h. The crucible was then taken out from the furnace for fast cooling to room temperature. Subsequently, the resulting black powder was consecutively washed with water and ethanol (Caution: the sample might burn into flames when washed with water for the first time), followed with the vacuum dry at 120 °C, which was termed TiO_{2-x}H_x. K/Ru/TiO_{2-x}H_x catalyst was then obtained using an impregnation method. First, TiO_{2-x}H_x was dispersed in a tetrahydrofuran solution of Ru₃(CO)₁₂ by stirring for 4 h under Ar atmosphere at room temperature. Then the suspension was vacuum dried at 40 °C to obtain the black powder. Next, the above black powder was heated by solar thermal energy at 300 °C for 4 h under Ar atmosphere and subsequently reduced by a reaction gas of N₂: 3H₂ (10 mL/min) at 360 °C for 1 h. The resulting Ru/TiO_{2-x}H_x powder was subsequently dispersed in an ethanol solution of KOH by stirring for 3 h at room temperature, followed with the vacuum dry at 120 °C, and finally heated at 360 °C by light in a reaction gas of N₂: 3H₂ (10 mL/min) for 1 h to obtain K/Ru/TiO_{2-x}H_x.

2.1.2. K/Ru/TiO₂, K/Ru/MgO and K/Ru/Al₂O₃

K/Ru/TiO₂ catalyst was synthesized with similar methods of K/Ru/TiO_{2-x}H_x only replacing the TiO_{2-x}H_x with TiO₂ (P25). K/Ru/MgO (Al₂O₃) catalyst were synthesized according to previous report [17]. MgO (Al₂O₃) was heated to 400 °C under vacuum, and then dispersed in a tetrahydrofuran solution of Ru₃(CO)₁₂ by stirring for 4 h at room temperature. After evaporating the solvent at 40 °C, the obtained powder was slowly heated to 450 °C (2 K/min) under vacuum. The resulting Ru/MgO (Ru/Al₂O₃) powder was dispersed in an ethanol solution of KOH under stirring for 3 h at room temperature, then collected for the subsequent vacuum dry at 120 °C, and finally heated by solar thermal energy at 400 °C in a reaction gas of N₂: 3H₂ (10 mL/min) for 4 h.

2.1.3. K/Ru/TiO_{2-x}H_x with various electron concentrations of TiO_{2-x}H_x (e₁, e₂, e₃ and e₄)

Herein e₄ was the K/Ru/TiO_{2-x}H_x catalyst used in the text. Samples of e₁, e₂ and e₃ were synthesized with similar procedures to e₄ except the Ru loading conditions. After evaporating the solvent of the Ru₃(CO)₁₂ and TiO_{2-x}H_x suspensions, the resulting powders were heated under ambient atmosphere by solar thermal energy at 360 °C, 330 °C and 300 °C for 2 h for e₁, e₂ and e₃, respectively. The concentrations of unpaired electrons of e₁, e₂, e₃ and e₄ were 4 × 10¹⁹/g, 7 × 10¹⁹/g, 1 × 10²⁰/g and 7 × 10²⁰/g, respectively.

2.1.4. K/Ru/TiO_{2-x}H_x@C

The mixture of NaBH₄ and TiO₂ was transferred into a crucible with cap under Ar purging, heated to 380 °C and maintained for 1 h in a furnace. The crucible was then taken out from the furnace for fast cooling to room temperature. Subsequently, the resulting black powder was thoroughly washed with the solution of water and ethanol (1:1, vol./vol.) to adsorb ethanol on its surface. Finally, the black powder

was vacuum dried at 60 °C and then transferred to the reaction cell and heated at 300 °C by solar thermal energy under N₂: 3H₂ atmosphere, which was called as TiO_{2-x}H_x@C. The Ru or K loading procedure was the same with that used for other supported Ru catalysts.

2.1.5. K/Ru/TiO_{2-x}H_x with various diameters of Ru ($D_{Ru} = 2.0\text{ nm}$, $D_{Ru} = 4.2\text{ nm}$ and $D_{Ru} = 7.9\text{ nm}$)

The catalyst of $D_{Ru} = 2.0\text{ nm}$ was the K/Ru/TiO_{2-x}H_x catalyst used in the text. Catalysts of $D_{Ru} = 4.2\text{ nm}$ and $D_{Ru} = 7.9\text{ nm}$ were synthesized with similar procedures to the catalyst of $D_{Ru} = 2.0\text{ nm}$ except the Ru loading conditions. After evaporating the solvent of the Ru₃(CO)₁₂ and TiO_{2-x}H_x suspensions, the resulting powders were heated by solar thermal energy at 450 °C and 540 °C for 0.5 h, and subsequently at 300 °C for another 3.5 h under Ar atmosphere for catalysts of $D_{Ru} = 4.2\text{ nm}$ and $D_{Ru} = 7.9\text{ nm}$, respectively.

2.2. Solar thermal ammonia synthesis

Solar thermal ammonia synthesis was carried out at ambient pressure in a designed quartz device. Power-tunable Xenon lamp (300 W, the light was concentrated ~9 times with a focus lens before use and its output light intensity was measured using an optical power meter) was used as simulated solar irradiation to trigger ammonia synthesis. Typically, 0.1 g catalyst was added into the quartz reactor with an area of 2 cm², and the light intensity was adjusted to maintain the catalysis temperature at ~360 °C, which was monitored by a catalyst-contact thermometer. The NH₃ generation was monitored by checking ammonia content in outlet gas absorbing solution (0.1 M HCl) with Nessler's reagent. On several occasions, we also qualitatively analyzed the inlet and outlet gas with gas chromatograph.

2.3. Sample characterization

The powder X-ray diffraction (XRD) measurements were recorded on a Rigaku D/MAX-RB diffractometer with monochromatized Cu K α radiation ($\lambda = 0.15418\text{ nm}$). Raman spectra were obtained by a confocal laser micro-Raman spectrometer (Thermo DXR Microscope, USA) with 532 nm laser. For the *in-situ* Raman measurements, samples were pressed to round plates (~0.1 g, with a radius of 0.35 cm) and then placed in a quartz reactor under the microscope. Electron paramagnetic resonance (EPR) spectra were conducted on a JEOL EMX EPR Spectrometer (Billerica, MA) at room temperature. 2, 2, 6, 6-tetramethylpiperidinyloxy (TEMPO) and Mn(II) were used as the standard sample and the reference sample for the quantitative analysis, respectively. ¹H MAS NMR experiments were performed on a Bruker Avance III 500 WB (11.75 T) spectrometer operating at a frequency of 500.58 MHz. A commercial DVT triple resonance H/X/Y 4.0 mm probe was used with a spinning frequency of 11.0 kHz. There is no proton background from the H/X/Y probe head and rotor caps. Solid-state ¹H MAS NMR spectra were recorded with a single pulse excitation, a 90° pulse length of 4.0 μs and a recycle delay of 4 s were applied to obtain quantitative results. Thermal conductivity of TiO_{2-x}H_x was measured by Hot disk TPS2500S with powder samples.

Transmission electron microscopy (TEM), high-resolution transmission electron microscopy (HRTEM), and scanning transmission electron microscopy (STEM) measurements were performed on Hitachi H-7650, JEOL-2010F and JEM-ARM200F, respectively, with an acceleration voltage of 200 kV. The resolution of STEM characterization is 80 pm with a probe aberration corrector. High-angular annular dark field (HAADF) images were acquired using a dwell time of 18.1 μs per pixel. The average particle size and size distribution of Ru were obtained by analyzing ~600 particles. UV-vis-NIR spectra of the samples were obtained using a UV-3600 plus spectrophotometer (Shimadzu, Japan) from 200 nm to 2500 nm. X-ray absorption spectroscopy (XAS) measurements were recorded at the beamline 1W1B of Beijing Synchrotron Radiation Facility, Institute of High Energy Physics,

Chinese Academy of Sciences. The X-ray absorption near-edge structure (XANES) spectra and extended X-ray absorption fine structure (EXAFS) spectra were processed using *Athena* (*Demeter*, 0.9.24) with standard procedures. X-ray photoelectron spectroscopy (XPS) data were obtained using a Thermo Scientific Escalab 250Xi and all binding energies were calibrated with $C_{1s} = 284.8$ eV. The Mott-Schottky experiments were conducted in an aqueous Na_2SO_4 solution (100 mL, 0.1 mol/L) using a CHI660B electrochemical work station. The FTO glass deposited with $1 \times 2 \text{ cm}^2$ samples was used as the working electrode. A platinum plate and a saturated calomel electrode (SCE) were used as the counter and the reference electrodes, respectively.

The contents of Ru in several catalysts were analyzed by inductively coupled plasma optical emission spectroscopy (ICP-OES) using a PerkinElmer Optima 5300 DV after samples dissolution according to standard in-house procedures. The CO-pulse chemisorption was conducted on an AutoChem II chemisorption analyzer (Micromeritics, USA). 0.1 g of samples were first heated to 400 °C under He atmosphere for 15 min, followed by H_2 reduction for 1 h and subsequent He purging for 1 h, and then cooled down to 50 °C in He atmosphere. The CO-pulse chemisorption was carried out under 50 °C.

FTIR spectra were recorded by Nicolet iS50 spectrometer (Thermo, USA) with a MCT detector in a designed reaction cell. Samples after reaction were pressed to round plates (~0.1 g, with the uniform radius of 0.35 cm) for measurement. First, a plate was heated to 400 °C in vacuum for 1 h and then treated with H_2 pulse (3.4 kPa) for six times, subsequently evacuated at 400 °C for 1 h to remove adsorbed hydrogen on Ru, and finally cooled down to room temperature in vacuum. The plate was exposed to 6.7 kPa N_2 to obtain the spectra of adsorbed N_2 at liquid nitrogen temperature. At room temperature, the spectra of NH_3 generation via N_2 reduction by H_{inc} in $K/Ru/TiO_{2-x}H_x$ was obtained when the plate was exposed to 6.7 kPa N_2 , subsequently the plate was heated to 260 °C in vacuum for 20 min to remove the absorbed NH_3 species and finally cooled down to room temperature for the next N_2 exposure. For H_{inc} -recycle (in $K/Ru/TiO_{2-x}H_x$) experiments, after every five times exposure of N_2 (a round), the plate was heated to 360 °C in vacuum, followed with H_2 pulse (3.4 kPa; six times) treatment for the H_{inc} -recycle via H-spillover.

2.4. Determination of x value in $Ru/TiO_{2-x}H_x$

We quantified the unpaired electron concentration of $Ru/TiO_{2-x}H_x$ using TEMPO and Mn(II) as the standard sample and the reference sample during the EPR measurement, respectively. Typically, TEMPO with unpaired electron number of 6.2×10^{16} and a certain amount of Mn(II) were first measured to obtain a standard EPR spectra. 0.1 g of sample and the same amount of Mn(II) were then measured under the same conditions. The unpaired electron concentration of the sample could therefore be obtained via the integral method of EPR peak areas. Then the idea of “ $F^+ \cdot H$ center” was adopted to determine the x value of $Ru/TiO_{2-x}H_x$ catalyst, i.e. an unpaired electron and an incorporated proton located on an oxygen vacancy [18]. In such a way, the x value of the $Ru/TiO_{2-x}H_x$ catalyst was estimated to be 0.19.

2.5. Determination of band edge positions of $TiO_{2-x}H_x$ and TiO_2

Bandgap (E_g) of TiO_2 was calculated from the UV-vis-NIR spectra. CB positions of $TiO_{2-x}H_x$ and TiO_2 (vs. SHE) were calculated by converting the flat-band potentials obtained from Mott-Schottky plots to CB positions (E_{CB}), because the flat-band potentials were usually ~0.1 eV higher than the flat-band potentials [19]. Relative VB positions of $TiO_{2-x}H_x$ and TiO_2 were determined by the VB-XPS. Then VB positions (vs. SHE) of $TiO_{2-x}H_x$ and TiO_2 were determined through $E_{VB} = E_{CB} - E_g$ [20]. Finally, the band edge positions (vs. physical scale) of $TiO_{2-x}H_x$ and TiO_2 were obtained by the SHE (V)-physical scale (eV) transformation via $E_{phys} = -(E_{SHE} + 4.44)$ [21].

2.6. DFT calculations and Wulff calculations of Ru

We used a similar method described in J. K. Nørskov's work to calculate the surface energies of Ru [4]. A Ru slab with a thickness between 7 and 9 Å and separated by a 10 Å vacuum was used. When n Ru atoms were exposed in each of the two surface sides of the slab, $2n$ atoms were set in the middle of the slab and kept frozen. The Monkhorst-Pack mesh was $8 \times 8 \times 1$ for Ru(001), and scaled accordingly for other surfaces. The surface energy is represented by $E_{surf} = (E_{tot} - N E_{bulk})/2A$, where N is the number of Ru atoms in the supercell, E_{tot} is the total energy, E_{bulk} is the total energy per atom of hcp Ru, and A is the surface area. The factor of 1/2 corresponds to two equivalent surface sides of the slab. Table S1 summarizes the surface energies (in J/m^2) for six Ru(hkl) surfaces with $h + k + l < 4$. There exist two structures for some of the (hkl) planes in an hcp Ru, labeled as A and B. The calculated surface energies were used for Wulff construction, based on which the Ru model of tetrakaidecahedron-like structure with monoatomic steps was constructed.

2.7. FDTD simulations

Simulations were performed using the software (Lumerical, Canada) of *FDTD Solutions* (8.15.736) for plasmonic near-field maps and *Device-Heat* (5.0.736) for temperature (T) profiles. The optical absorption data calculated by *FDTD Solutions* was used as heat input for the temperature simulation. The electromagnetic field (MF) enhancement and T increasing results were the average value of 22 wavelengths and 4 wavelengths simulations, respectively, based on a model of TiO_2 supported Ru cluster (the morphology of Ru was close to the Wulff construction). The minimum mesh interval for MF and T simulations were set as 0.08 nm and 0.01 nm, respectively. Because of the black color and difficulty in preparing smooth thin films of $TiO_{2-x}H_x$, precise measuring its optical constants was quite difficult. Here for the purpose of just confirming the confined energy around Ru, we used the optical constants of TiO_2 for the simulation of $TiO_{2-x}H_x$ with a minimum of assumption, neglecting the light adsorption of $TiO_{2-x}H_x$ in the Vis-IR region, and thus the confined energy would be underestimated in this way. The material parameters of the TiO_2 and Ru were obtained from the Palik data [22,23]. To assess the reliability of T simulation results, a relation bridging simulation and real condition together was set as below: if the TiO_2 4 μm away from the Ru-TiO₂ interface was set to be 20 °C, the Ru-TiO₂ interface could reach a temperature in the range of 320–420 °C by the 425 nm (its T simulation result was close to the average value in the range of sunlight) light input, matching the solar thermal heating effect of 360 °C measured in real experiments.

3. Results and discussion

3.1. Synthesis and characterization of disordered $TiO_{2-x}H_x$ with abundant electrons and protons

In the $K/Ru/TiO_{2-x}H_x$ catalyst, support with abundant localized electrons states is vital for the solar thermal ammonia synthesis with Ru, not only by enhancing solar absorption, but also by promoting the Ru LSPR and facilitating the N_2 activation. Localized electronic states on metal oxides are commonly reported by generating V_{OS} . However, the preservation of abundant V_{OS} is very difficult for crystalline metal oxides because of their strong electron confinement and structure distortion [18], so we synthesized a black $TiO_{2-x}H_x$ support of disordered nature to stabilize abundant V_{OS} , which was prepared from crystalline TiO_2 (Degussa P25) by a solid $NaBH_4$ reduction and fast cooling method.

TEM images revealed the morphology change from TiO_2 nanoparticles to distorted $TiO_{2-x}H_x$ nanosheets (Fig. S1a and S1b). HRTEM images indicated that the lattice of $TiO_{2-x}H_x$ was disordered in comparison with its precursor of crystalline TiO_2 (Fig. 1a and b). The XRD

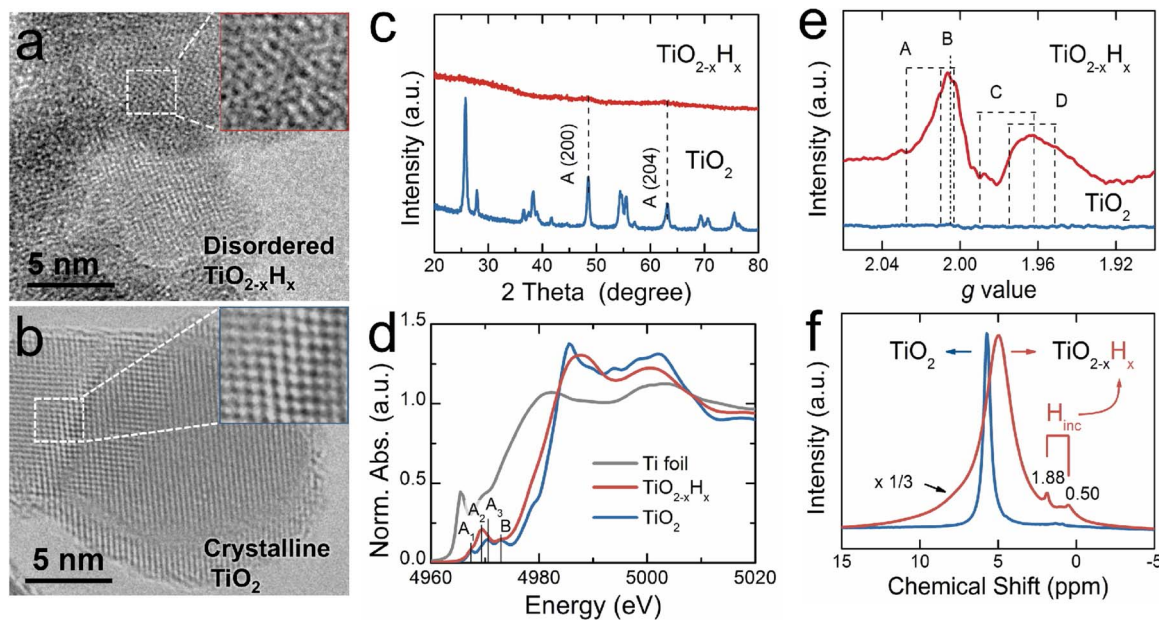


Fig. 1. Characterizations of the disordered $\text{TiO}_{2-\text{x}}\text{H}_\text{x}$. HRTEM images of the disordered $\text{TiO}_{2-\text{x}}\text{H}_\text{x}$ (a) and crystalline TiO_2 (b). (c) XRD patterns, (d) the normalized Ti K-edge XANES spectra, (e) EPR spectra and (f) ^1H NMR spectra of the disordered $\text{TiO}_{2-\text{x}}\text{H}_\text{x}$ and crystalline TiO_2 .

patterns of $\text{TiO}_{2-\text{x}}\text{H}_\text{x}$ exhibited its disordered lattice in the long-range, with only two weak peaks ((200) and (204) of anatase, PDF NO. 02-0406) indicative of TiO_2 phases, while P25 TiO_2 was a mixture of anatase (PDF NO. 02-0406) and rutile (PDF NO. 88-1174) (Fig. 1c). In the Raman spectra, the peaks of $\text{TiO}_{2-\text{x}}\text{H}_\text{x}$ broadened and blue shifted in comparison with that of TiO_2 . Additionally, new bands at 259, 761, 832 and 920 cm^{-1} emerged for $\text{TiO}_{2-\text{x}}\text{H}_\text{x}$ (Fig. S1c). These features indicated the phonon confinement effect in the $\text{TiO}_{2-\text{x}}\text{H}_\text{x}$ sample, which might arise from the finite-size effects (with grains $< 10 \text{ nm}$) and/or the presence of defects. As we did not observe finite-size $\text{TiO}_{2-\text{x}}\text{H}_\text{x}$ grains ($< 10 \text{ nm}$) in the TEM and HRTEM images (Fig. 1a and S1a), and thus concluded that the short-range lattice disorder of $\text{TiO}_{2-\text{x}}\text{H}_\text{x}$ stemmed from the presence of defects [24]. Meanwhile, Ti K-edge XANES spectra of $\text{TiO}_{2-\text{x}}\text{H}_\text{x}$ possessed four TiO_2 peaks (labeled as A_{1-3} and B). The peak A_2 was larger than that of TiO_2 , indicative of a typical amorphous structure of unsymmetrically distorted Ti–O bonds in $\text{TiO}_{2-\text{x}}\text{H}_\text{x}$ (Fig. 1d) [25]. Moreover, the edge of $\text{TiO}_{2-\text{x}}\text{H}_\text{x}$ XANES spectra was between those of Ti foil and TiO_2 , suggesting that the valence of Ti atoms in $\text{TiO}_{2-\text{x}}\text{H}_\text{x}$ was between 0 and +4 after reduction. The reduction induced coordination changes were further reflected by the EXAFS spectra (Fig. S1d). The main peak at $\sim 1.5 \text{ \AA}$ from Ti–O bond, the minor peak at $\sim 2.5 \text{ \AA}$ from Ti–Ti bond, and the third and higher peaks attributed to multiple scattering, were observed on both $\text{TiO}_{2-\text{x}}\text{H}_\text{x}$ and TiO_2 . Specifically for $\text{TiO}_{2-\text{x}}\text{H}_\text{x}$, the peaks assigned to Ti–O and Ti–Ti were broadened and the fraction of the first peak (Ti–O) was reduced because of O loss, and the fraction of the third and higher peaks were reduced because of heterogeneous broadening, in comparison with those of TiO_2 . These changes clearly indicated the disordered nature of $\text{TiO}_{2-\text{x}}\text{H}_\text{x}$ with V_{OS} [26].

The V_{OS} of $\text{TiO}_{2-\text{x}}\text{H}_\text{x}$ were further confirmed by room temperature EPR results. EPR signals of $1.90 < g < 2.06$ could at least be assigned to four species: $\text{Ti}^{4+}\text{-O}_2\text{ }^-$ with $[g_1 \ g_2 \ g_3] = [2.028 \ 2.010 \ 2.003]$ (A), e^- trapped at V_{OS} with $g = 2.005$ (B), anatase Ti^{3+} with $[g_1 \ g_2 \ g_3] = [1.990 \ 1.990 \ 1.962]$ (C), and rutile Ti^{3+} with $[g_1 \ g_2 \ g_3] = [1.975 \ 1.975 \ 1.951]$ (D) (Fig. 1e). All these species confirmed the formation of V_{OS} [27]. Usually, unpaired electrons on V_{OS} were detectable only under low temperatures such as 77–100 K, if the concentrations of V_{OS} was low. The detectable EPR signals of $\text{TiO}_{2-\text{x}}\text{H}_\text{x}$ under room temperature indicated that disordered $\text{TiO}_{2-\text{x}}\text{H}_\text{x}$ was able to stabilize abundant excess electrons, which might be arisen from the charge-balancing ability of

incorporated H atoms (H_{inc}) near unpaired electrons [18,28]. The presence of H_{inc} was confirmed by ^1H MAS NMR results (Fig. 1f). In the ^1H NMR spectra of $\text{TiO}_{2-\text{x}}\text{H}_\text{x}$, besides the main peak around 5 ppm (5.72 ppm for crystalline TiO_2 and 4.99 ppm for disordered $\text{TiO}_{2-\text{x}}\text{H}_\text{x}$) assigned to adsorbed water or Ti–OH groups, two additional narrow ^1H NMR peaks at 1.88 and 0.50 ppm confirmed the existence of incorporated H in $\text{TiO}_{2-\text{x}}\text{H}_\text{x}$ with dynamic nature [29,30]. These H dopants might be originated from the *in-situ* formed active H during NaBH_4 decomposition under reduction [16,31]. Obviously, this almost completely disordered $\text{TiO}_{2-\text{x}}\text{H}_\text{x}$ with abundant V_{OS} and H_{inc} is different from all the hydrogenated TiO_2 or black TiO_2 counterparts reported previously [14,17,32,33], and may therefore efficiently tune the electronic structure of Ru through the electron donation from V_{OS} and enhance the LSPR of Ru via plasmon hybridization effect for highly efficient Ru-catalysts.

3.2. Assembly and characterization of the (K/Ru)/ $\text{TiO}_{2-\text{x}}\text{H}_\text{x}$ catalyst

We utilized the selective metal deposition ability of V_{OS} in $\text{TiO}_{2-\text{x}}\text{H}_\text{x}$ to assemble K/Ru/ $\text{TiO}_{2-\text{x}}\text{H}_\text{x}$ with an impregnation method [34]. The HAADF-STEM and HRTEM images of K/Ru/ $\text{TiO}_{2-\text{x}}\text{H}_\text{x}$ revealed that the lattices of $\text{TiO}_{2-\text{x}}\text{H}_\text{x}$ support were still disordered, and Ru nanocrystals were highly dispersed onto the disordered $\text{TiO}_{2-\text{x}}\text{H}_\text{x}$ surface with an average diameter of 2.0 nm. The step B_5 sites capable of efficient N_2 activation were observed on the supported Ru, which was embedded in disordered $\text{TiO}_{2-\text{x}}\text{H}_\text{x}$ matrix (Fig. 2a–c, Table S1) [4]. Energy dispersive X-ray (EDX) mapping and XRD patterns also confirmed the successful deposition of Ru on $\text{TiO}_{2-\text{x}}\text{H}_\text{x}$ (Fig. 2d and S2a). The Ru/ $\text{TiO}_{2-\text{x}}\text{H}_\text{x}$ could absorb the whole UV-vis-NIR region of the sunlight (Fig. 2e), partially because the electron concentration was as high as $\sim 7 \times 10^{20}/\text{g}$ in the Ru/ $\text{TiO}_{2-\text{x}}\text{H}_\text{x}$ ($x = 0.19$) (Fig. 2f), which could donate electrons to Ru for the efficient solar utilization. The electron donation was embodied by the promoted electronic structure of Ru, which was verified by XAS and XPS. The near-edge of Ru/ $\text{TiO}_{2-\text{x}}\text{H}_\text{x}$ XANES spectra (Ru K-edge) was slightly shifted to lower energies compared with the spectra of Ru foil, away from the spectra of RuO_2 , indicating the supported Ru was of negative charges due to its electron-rich nature (Fig. 2g). Valence band (VB) XPS further confirmed the electronic structure of $\text{TiO}_{2-\text{x}}\text{H}_\text{x}$ supported Ru. Ru, Ru/ $\text{TiO}_{2-\text{x}}\text{H}_\text{x}$ and Ru/ TiO_2 exhibited the VB edge positions of -0.79 , -0.95 and -0.75 eV , respectively, suggesting the

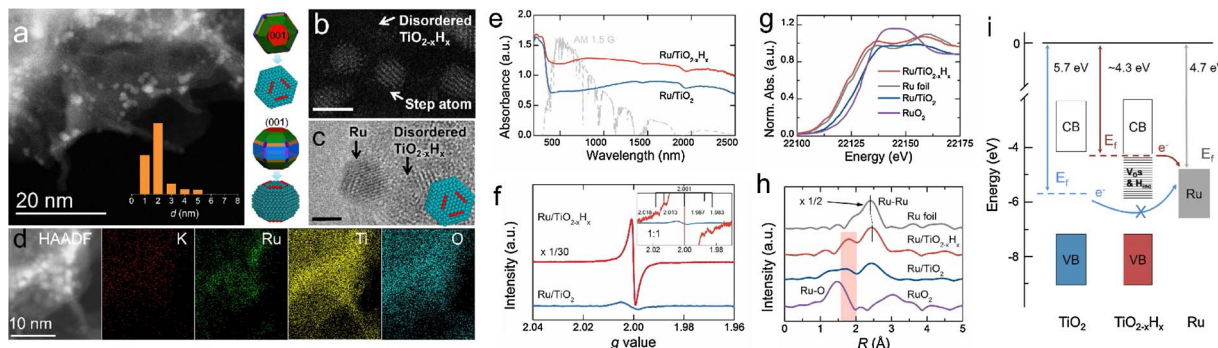


Fig. 2. Characterizations of the (K/Ru/TiO_{2-x}H_x) catalyst. HAADF-STEM image (a, b) and HRTEM image (c) of K/Ru/TiO_{2-x}H_x. Inset: Wulff construction (the faces of (001), (100), (101), (201), (111) and (210) were labeled as red, blue, green, orange, purple and pink, respectively) based atomic Ru model (step B₅ sites were shown in red) matching the actual Ru particle. Scale bars are 2 nm. (d) HAADF image and EDX mapping confirmed the composition of the K/Ru/TiO_{2-x}H_x catalyst. (e) Diffuse reflectance spectra, (f) room temperature EPR spectra (zoomed; inset is the 1:1 spectra), (g) XANES spectra and (h) EXAFS spectra of TiO₂ and TiO_{2-x}H_x supported Ru catalyst. (i) Energy alignment of the Fermi levels (E_f) for TiO₂, TiO_{2-x}H_x, and Ru. (For interpretation of the references to colour in this figure legend, the reader is referred to the web version of this article.)

electron donation from localized electron states in TiO_{2-x}H_x support to Ru (Fig. S2b). In addition, the EXAFS spectra (Fig. 2h) of Ru/TiO_{2-x}H_x revealed its longer Ru–Ru bond than that of Ru foil because electron-rich Ru atoms would suffer from electrostatic repulsion, further confirming the strong electron donation from TiO_{2-x}H_x support to Ru. Given that V_Os and incorporated H (H_{inc}) induced localized states were 0–1.5 eV below the conduction band (CB) of TiO_{2-x}H_x [16,32,33], the Fermi level of TiO_{2-x}H_x was supposed to largely shift up and thus be above that of Ru, so localized electrons on TiO_{2-x}H_x could transfer to Ru via the Ru–O or Ru–Ti bonds at the Ru/TiO_{2-x}H_x interface (Fig. 2i and S3). These bonds formed between Ru and TiO_{2-x}H_x were reflected by the small peak at ~1.8 Å in the EXAFS spectra of Ru/TiO_{2-x}H_x (Fig. 2h) [35].

3.3. Solar thermal ammonia synthesis

With only 300 W Xe lamp irradiation, this K/Ru/TiO_{2-x}H_x (3 wt% Ru) catalyst reached a reaction temperature of 360 °C within 13 min, and delivered an amazing NH₃ generation rate of 112.6 μmol g⁻¹ h⁻¹ at the gas flow rate of 6 mL/min (at a TOF of 3.9 × 10⁻⁴ s⁻¹), 140.7 and 6.7 times those of K promoted Ru/Al₂O₃ and Ru/MgO at 360 °C under thermal heating without solar light irradiation (Fig. 3a, b and S4), and similar to the Haber-Bosch process, its reactivity or TOF value could enhance with the elevated gas flow rate (its TOF could be as high as 1.65 × 10⁻³ s⁻¹ when proceeds at 120 mL/min), which was comparable to those of conventional thermal catalysis (Table S2 and S3). However, no ammonia was generated on crystalline TiO₂ supported Ru. More interestingly, we found that the reactivity of K/Ru/TiO_{2-x}H_x was positively associated with the unpaired electrons concentration of TiO_{2-x}H_x support (Fig. 3c), further confirming the critical role of electron donation from the TiO_{2-x}H_x support to Ru. Subsequently, we compared the activities of thermal and solar thermal process on K/Ru/TiO_{2-x}H_x at 360 °C, and found that the activity of solar thermal catalysis of K/Ru/TiO_{2-x}H_x was about twice that of its thermal catalysis under the same temperature (Fig. 3d), and this solar thermal ammonia synthesis activity could last for more than 7 h, much longer than that (~4 h) of thermal synthesis. Moreover, we discovered the reactivity decrease of solar thermal ammonia synthesis could be recovered via switching off the light every 7 h, while that for thermal catalysis could not be recovered (Fig. 3e).

3.4. The surface disorder associated reactivity of K/Ru/TiO_{2-x}H_x

To understand the reactivity decrease and regeneration in Fig. 3d and 3e, we analyzed the structure change of K/Ru/TiO_{2-x}H_x during the reaction. We first examined the catalyst after different reaction time by XRD. No matter under solar thermal catalysis or

thermal catalysis, all XRD patterns demonstrated similar small Ru peaks and amorphous nature of the TiO_{2-x}H_x support (Fig. 4a). Then the Raman spectra, which is sensitive to local and surface structure change, was applied to *in-situ* monitor the K/Ru/TiO_{2-x}H_x. In the Raman spectra, E_g peak of TiO_{2-x}H_x (145.2 cm⁻¹) red shifted to 142.2 cm⁻¹ along with reaction time under thermal catalysis, accompanied by the narrowed peak width, while that for solar thermal catalysis maintained around 145.2 cm⁻¹ with similar broad peak (Fig. 4b; measured upon light off after reaction for 7 h). Given that narrow E_g band centered at ~142 cm⁻¹ was the typical character of crystalline TiO₂, the above results suggested the surface of K/Ru/TiO_{2-x}H_x reconstructed to crystalline K/Ru/TiO₂ after thermal catalysis, while maintained its disordered structure after light off during solar thermal catalysis. As both reactivity results and energy diagram indicated that the TiO_{2-x}H_x supported Ru was more reactive than the TiO₂ supported Ru because of the electron donation (Figs. 3b and 4c), the K/Ru/TiO_{2-x}H_x catalyst deactivated upon its surface reconstructed to K/Ru/TiO₂ after reaction. This result indicated that the key to high-performance K/Ru/TiO_{2-x}H_x was to stabilize the disordered TiO_{2-x}H_x. So an optimized catalyst could be obtained using a stable TiO_{2-x}H_x@C support, which composed of partially coated carbon layers (act as stabilizer and electron shuttle [36]) on the surface of TiO_{2-x}H_x, and the reactivity of K/Ru/TiO_{2-x}H_x@C could last for more than 40 h without obvious decrease (Fig. 4d and S5).

3.5. Ammonia synthesis mechanism of K/Ru/TiO_{2-x}H_x

To demystify the superior reactivity of K/Ru/TiO_{2-x}H_x, we investigated the adsorbed state of N₂ on catalyst surface and the reaction kinetics. At liquid N₂ temperature, the Fourier transform infrared (FTIR) spectra of N₂ adsorption on K/Ru/TiO_{2-x}H_x gave a peak at 2147 cm⁻¹ (corresponding to the N–N stretching peak of chemisorbed N₂). The replacement of ¹⁴N₂ with ¹⁵N₂ caused a red shift of IR peak position from 2147 cm⁻¹ to 2079 cm⁻¹. This isotopic shift was close to the theoretic value (2147/2079 = 1.03 vs. (15/14)^{1/2} = 1.04), confirming that these species were adsorbed N₂. The N₂ adsorption peak on K/Ru/TiO_{2-x}H_x (2147 cm⁻¹) was lower than those of K/Ru/Al₂O₃ (2258 cm⁻¹) or K/Ru/MgO (2180 cm⁻¹), indicative of the further N≡N weakening by excess electrons in the TiO_{2-x}H_x (Fig. 5a) [37]. Unprecedentedly, when we tried to examine the N₂ adsorption at room temperature, N₂ was reduced to NH₃ by H_{inc} of TiO_{2-x}H_x in the K/Ru/TiO_{2-x}H_x catalyst rather than adsorption (Fig. 5b). We did not detect any ammonia in the reaction cell under room temperature (Table S2), probably because high energy was needed for the NH₃ desorption. The narrow peak around 1633 cm⁻¹ was the δ_{as} of NH₃, and the broad peak from 2711 to 3725 cm⁻¹ could be assigned to the ν_a and ν_{as} of NH_x (x = 1–3) in the region of 2711–3110 cm⁻¹ and the ν_{as} two peaks of NH₃ at 3308 and 3461 cm⁻¹ [38]. These δ_{as} and ν_{as} peaks, in

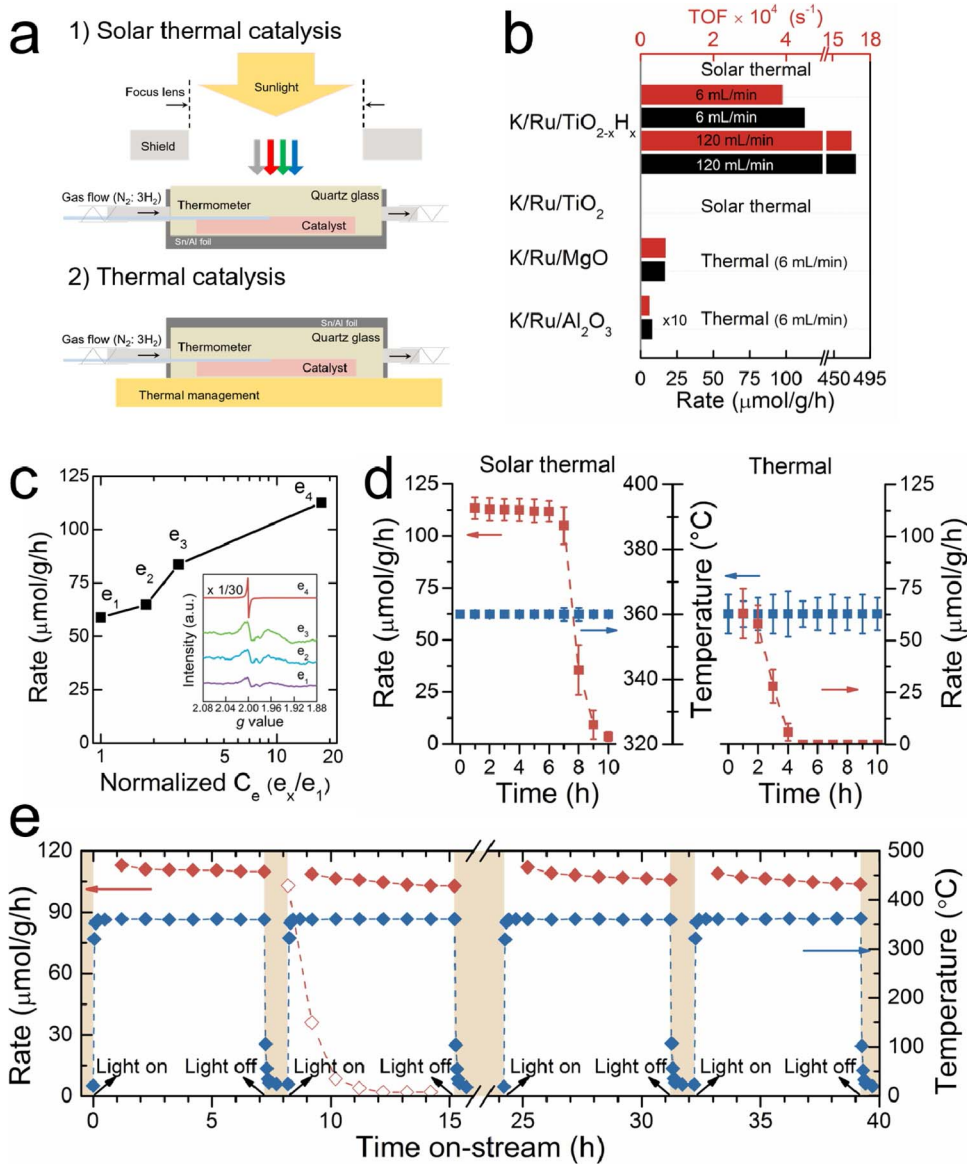


Fig. 3. Catalytic performances. (a) Catalytic devices. (b) Comparison of ammonia synthesis rates of four Ru catalysts at 360 °C. (c) Ammonia synthesis rate of four K/Ru/TiO_{2-x}H_x catalysts with different x values (inset: EPR spectra of the four catalysts). (d) Difference in ammonia yields for thermal and solar thermal catalysis under the same temperature with K/Ru/TiO_{2-x}H_x. In both cases the catalyst was maintained for 1 h before collecting the activity data. (e) Time dependence of reaction activity over K/Ru/TiO_{2-x}H_x. Curve with open diamonds demonstrated the activity loss if the catalyst was not treated with fast cooling at 7 h.

conjunction with the two weak peaks at 3404 and 3350 cm^{-1} which might be assigned to the metal-NH_x species (Fig. 5c and 5d) [39], indicated the formation of Ti-NH_x species on the K/Ru/TiO_{2-x}H_x catalyst. Isotopic experiments with peak shifts (3308 cm^{-1} –3175 cm^{-1} and 1633 cm^{-1} –1552 cm^{-1}) further confirmed these assignments (Fig. 5e). This room temperature NH₃ generation was exclusively observed on K/Ru/TiO_{2-x}H_x, while no NH₃ was generated on K/Ru/Al₂O₃, K/Ru/MgO or K/Ru/TiO₂ under the same condition (Fig. S6), indicating the essential role of H in TiO_{2-x}H_x during this room temperature ammonia generation via nitrogen activation. Moreover, the NH₃ generation amounts gradually decreased during the subsequent N₂ exposure experiments on K/Ru/TiO_{2-x}H_x (Fig. 5b), suggesting the consumption of incorporated H in the K/Ru/TiO_{2-x}H_x catalyst. Therefore, we suppose that the TiO_{2-x}H_x support in the catalyst could efficiently store and provide reversible H_{inc} for the ammonia synthesis, which was further validated by the H_{inc} regeneration experiments through H-spillover from Ru. The reduced NH₃ generation could be recovered if the catalyst was treated by H₂ at elevated temperature again (Fig. S7). These results solidly evidenced that N₂ was activated on Ru and the spillover of H atoms on Ru strongly contributed to the regeneration of H_{inc} in the K/Ru/TiO_{2-x}H_x catalyst. Different from the photocatalytic nitrogen fixation in solution (N₂ + 6H⁺ + 6e⁻ → 2NH₃) observed on TiO₂ of V_{OS},

which was initiated by the N–N triple bond elongation on V_{OS} via the injection of photo-generated electrons [40], TiO_{2-x}H_x alone could not reduce N₂ into NH₃ in the absence of Ru via N₂ + 3H₂ → 2NH₃, because this reaction was triggered by the N–N triple bond dissociation on some zero-valent transition metals, and TiO_{2-x}H_x was not active for N₂ dissociation although it had abundant V_{OS} and H_{inc}. Therefore, ammonia was produced on the Ru surface via a commonly accepted mechanism (mechanism I, Fig. 5f) [4], and also via the reaction between N activated by Ru and H_{inc} on the TiO_{2-x}H_x surface (mechanism II, Fig. 5f). Although the H atoms in electrides or metal hydrides could react with the activated N₂ [5,21,41–44], the discovery of H_{inc} in the TiO_{2-x}H_x to react with Ru activated N₂ was still significantly different from these previously reported ammonia synthesis mechanisms, because it could take place under room temperature, indicating a reaction pathway of extremely low activation barriers. In this novel solar thermal ammonia synthesis process (mechanism II), the involvement of H_{inc} could avoid the active sites saturation by adsorbed H atoms on Ru and thus prevent the H₂ poisoning of electronically promoted Ru, as confirmed by the much higher reaction order (−0.14) of H₂ on K/Ru/TiO_{2-x}H_x than that (−0.84) on K/Ru/MgO. Meanwhile, the reaction order of N₂ on K/Ru/TiO_{2-x}H_x was as low as 0.38, revealing the catalyst was highly efficient for the N₂ activation (Fig. 5g, Table S4), consistent

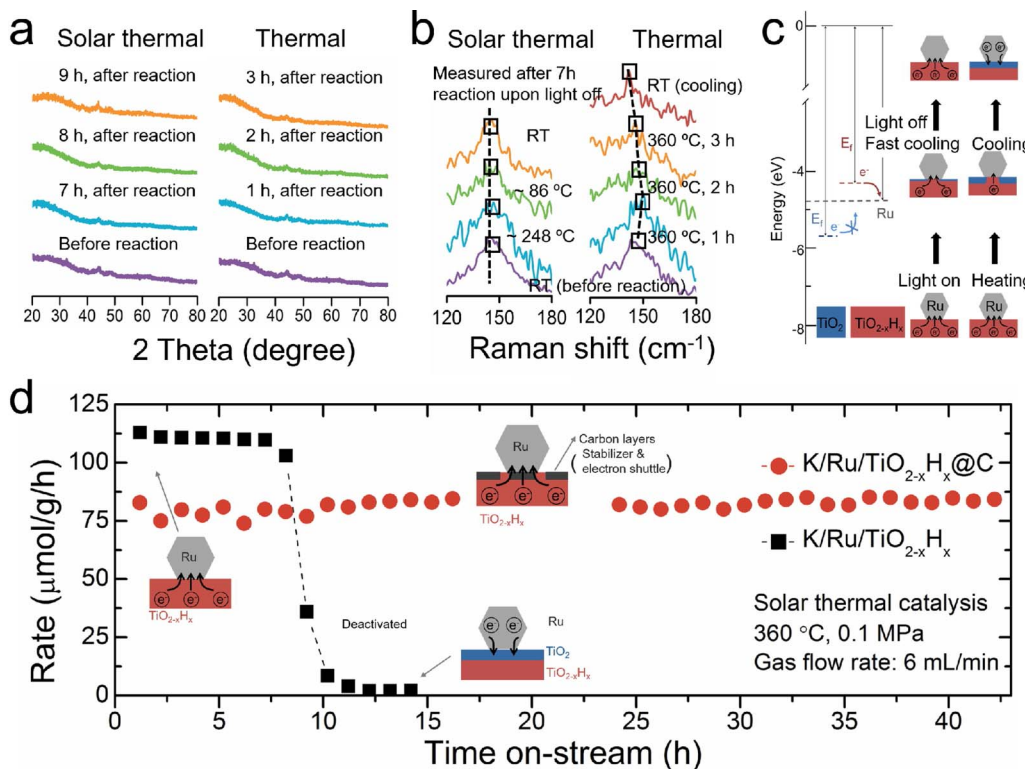


Fig. 4. The surface disorder associated reactivity over K/Ru/TiO_{2-x}H_x. (a) XRD patterns of K/Ru/TiO_{2-x}H_x catalyst after solar thermal (left) or thermal (right) catalysis with different reaction time. (b) *In-situ* Raman spectra of the most intense E_g peak of TiO_{2-x}H_x in K/Ru/TiO_{2-x}H_x under solar thermal (left; measured at 1, 2 and 20 min after light off) and thermal (right) catalytic ammonia synthesis. (c) Fermi levels of TiO₂, TiO_{2-x}H_x and Ru, and the proposed mechanism of surface disorder associated reactivity. (d) Time dependence of the reactivity over K/Ru/TiO_{2-x}H_x@C and K/Ru/TiO_{2-x}H_x (inset: proposed mechanism of surface disorder associated reactivity over the catalysts).

with the FTIR N₂ adsorption results.

To delineate the superiority of solar thermal catalysis over conventional thermal catalysis under the same temperature, we first measured their apparent activation energies. The value for solar thermal ammonia synthesis was 65 KJ/mol, lower than that (86 KJ/mol) of thermal catalysis (Fig. 6a, Table S4), which meant solar thermal ammonia synthesis proceeded with lower energy barrier than thermal counterpart. This difference might arise from the light induced confined

energy because of the plasmonic effects. Then we carried out FDTD simulations to monitor the confined energy (localized MF and heat) of Ru/TiO_{2-x}H_x after light irradiation (Fig. S8a). Similar with previous report, Ru generated a ~6 times enhancement of localized MF normalized to the incident field ($|E/E_0|^2$) (Fig. 6b) [16]. Unexpectedly, this Ru/TiO_{2-x}H_x catalyst delivered an excellent light-to-heat transformation, as the synthesized TiO_{2-x}H_x had a low thermal conductivity of 0.126 W/mK, the generated heat on Ru was not easy to spread to TiO₂.

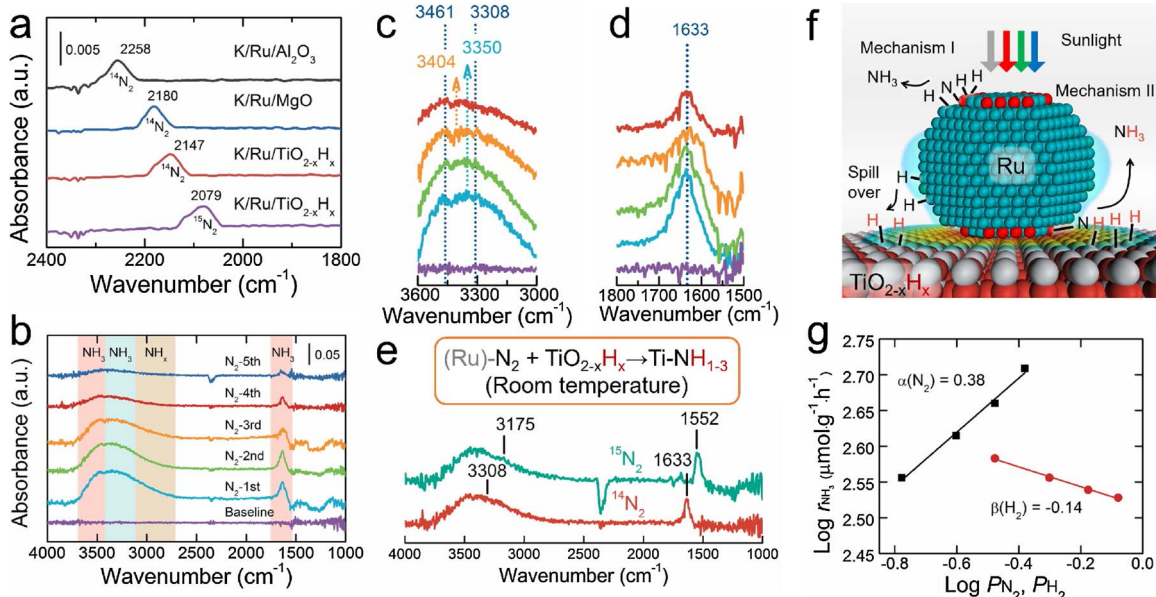


Fig. 5. Mechanism study of ammonia synthesis over the K/Ru/TiO_{2-x}H_x catalyst. (a) FTIR spectra of adsorbed N₂ at various supported Ru catalysts (K/Ru = 1) at liquid N₂ temperature. (b) *In-situ* FTIR spectra of room temperature NH₃ generation via N₂ reduction on K/Ru/TiO_{2-x}H_x catalyst, and corresponding enlarged spectra in the range of 3000 cm⁻¹–3600 cm⁻¹ (c) and 1500 cm⁻¹–1800 cm⁻¹ (d). (e) Isotopic experiments of room temperature N₂ reduction. (f) Schematic illustration of solar thermal ammonia synthesis on Ru/TiO_{2-x}H_x. The atomic size of Ru (blue) corresponding to Ti (grey) and O (brown) atoms was reduced for presentation, B₅ sites were shown in red. (g) Reaction rates (r_{NH_3}) as a function of N₂ and H₂ partial pressure over K/Ru/TiO_{2-x}H_x with a total gas flow rate of 60 mL/min. (For interpretation of the references to colour in this figure legend, the reader is referred to the web version of this article.)

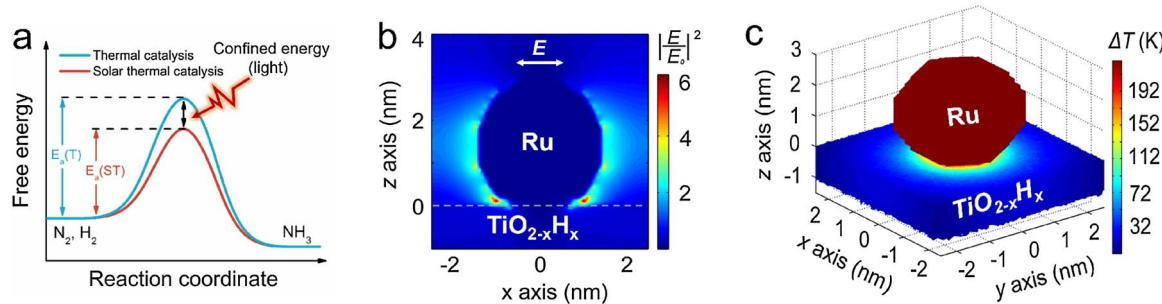


Fig. 6. Role of light induced confined energy. (a) Energy difference between thermal catalysis and solar thermal catalysis. (b) 2D near field intensity normalized to the incident field irradiated by sunlight and (c) 3D temperature profile irradiated by $\lambda = 425$ nm (whose T simulation result was close to the average value in the range of sunlight) around supported Ru cluster.

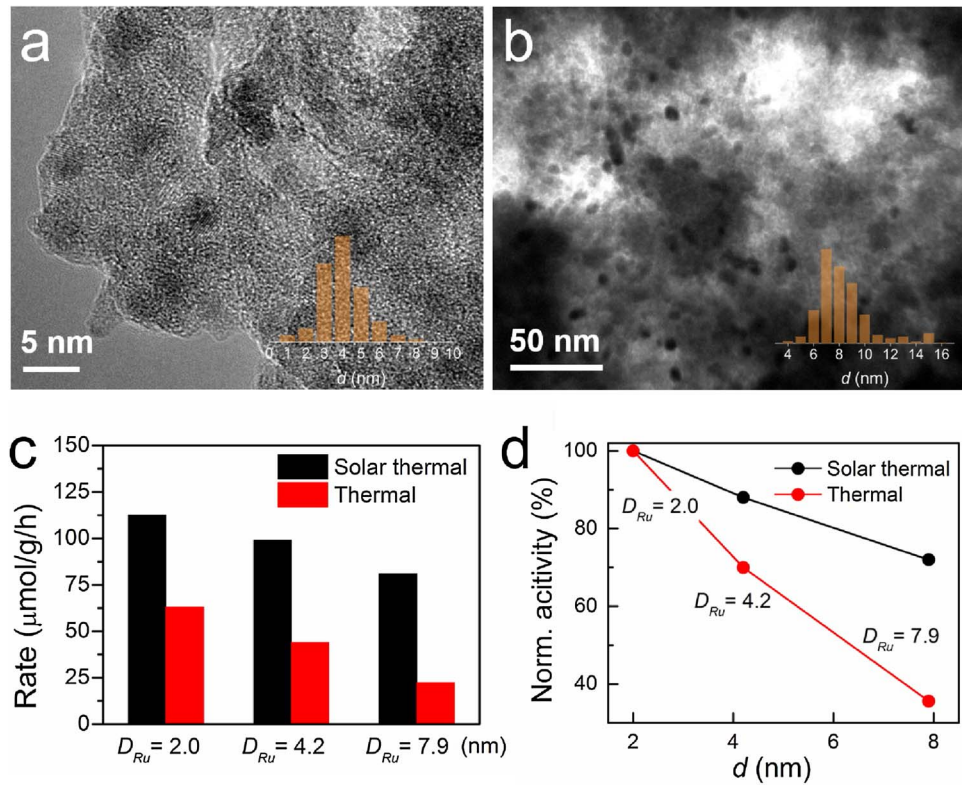
xH_x or to air (thermal conductivity: 0.026 W/mK), resulting in a super high accumulation of localized temperature (~ 190 °C) on Ru (Fig. 6c and S8b), which meant the temperature of Ru exceeded the average catalyst temperature of 360 °C by 20–100 °C under solar thermal catalysis, while the temperature of $\text{TiO}_{2-x}\text{H}_x$ was lower than the average catalyst temperature. The temperature of K/Ru/ $\text{TiO}_{2-x}\text{H}_x$ was found to significantly affect its stability because of $\text{TiO}_{2-x}\text{H}_x$ reconstruction. Although K/Ru/ $\text{TiO}_{2-x}\text{H}_x$ delivered better activities at higher temperature, it deactivated very quickly (Fig. S9). Therefore, the relatively lower catalyst temperature under light irradiation might retard the reconstruction of $\text{TiO}_{2-x}\text{H}_x$ in comparison with the case of thermal heating. Moreover, given both MF and heat could generate energetic electrons to overcome energy barriers [15], we suppose this light induced confined energy accounts for the reduced activation energy and better reactivity of solar thermal catalysis than thermal catalysis. This deduction was further validated by the B_5 amounts-reactivity relationship. When reducing the B_5 sites by increasing the diameter of supported Ru particle in the Ru/ $\text{TiO}_{2-x}\text{H}_x$ catalyst (from 2.0 nm, 4.2 nm to 7.9 nm), thermal catalysis demonstrated a typical activity drop to decreased B_5 sites [45]. Solar thermal catalysis also showed decrease activity, but less sensitive to the B_5 amount (Fig. 7). This less B_5 -

reactivity dependence could be explained by the size effect of plasmonics [46]. As light absorbance increased along with the increased Ru particle size, the energy confinement became more intensive to compensate the activity loss of reduced B_5 sites when enlarging the Ru size.

4. Conclusions

In conclusion, we have realized Haber-Bosch comparable reactivity via solar ammonia synthesis from N_2 and H_2 using the K/Ru/ $\text{TiO}_{2-x}\text{H}_x$ catalyst, which uses solar energy as the only energy input. The catalyst absorbs sunlight in the whole UV-vis-NIR region and then delivers an efficient solar-to-thermal transformation to drive ammonia synthesis. Different from thermal catalysis, this solar thermal strategy further confined electromagnetic and thermal energy in small volume around Ru cluster because of LSPR, exhibiting reduced activation energy and enhanced reactivity. Within the catalyst, $\text{TiO}_{2-x}\text{H}_x$ support of abundant $\text{V}_{\text{O}}\text{s}$ and H_{inc} has the electron/proton reservoir ability, enabling Ru to be electron-rich for efficient N_2 activation, and also providing H_{inc} to react with Ru activated N_2 to form NH_3 even at room temperature (Mechanism II). This new mechanism promotes the Ru adsorbed H, which is the origin of H_2 poisoning for Ru catalyst during the

Fig. 7. Ru particle size associated reactivity. HRTEM and TEM images of K/Ru/ $\text{TiO}_{2-x}\text{H}_x$ with the average Ru diameter of 4.2 nm ($D_{\text{Ru}} = 4.2$; a) and 7.9 nm ($D_{\text{Ru}} = 7.9$; b), respectively. (c) Comparison of NH_3 generation rates with three K/Ru/ $\text{TiO}_{2-x}\text{H}_x$ catalysts of different Ru size under solar thermal and thermal catalysis and (d) the corresponding normalized reactivity (to the reactivity of $D_{\text{Ru}} = 2.0$) as a function of Ru particle size.



conventional thermal ammonia synthesis, to transfer to the $\text{TiO}_{2-x}\text{H}_x$ support for the subsequent NH_3 generation. More importantly, the H_{inc} involved mechanism II can realize NH_3 generation with low energy barriers under room temperature, suggesting its promising application potential. Through this mechanism II, in conjunction with the confined energy induce by LSPR, we offer a new strategy towards a mild and efficient ammonia synthesis.

Acknowledgements

This work was supported by National Natural Science Funds for Distinguished Young Scholars (Grant 21425728), National Basic Research Program of China (973 Program) (Grant 2013CB632402), National Key Research and Development Program of China (Grant 2016YFA0203002), National Science Foundation of China (Grant 51472100), and Graduate Education Innovation Funding Project Grant from CCNU (2016CXZZ54). We thank Dr. Liying Wang and Dr. Liting Luo (National Center for Magnetic Resonance in Wuhan) for the solid-state NMR and EPR characterization of samples. We also thank the National Supercomputer Center in Jinan for providing high performance computation.

Appendix A. Supplementary data

Supplementary data associated with this article can be found, in the online version, at <http://dx.doi.org/10.1016/j.apcatb.2017.11.010>.

References

- [1] R. Schlögl, Handbook of heterogeneous catalysis, in: G. Ertl, H. Knözinger, J. Weitkamp (Eds.), *Ammonia Synthesis*, Wiley-VCH, Weinheim, 1997, pp. 1697–1745.
- [2] R. Schlögl, Catalytic synthesis of ammonia—A never-ending story? *Angew. Chem. Int. Ed.* 42 (2003) 2004–2008.
- [3] G. Ertl, Reactions at surfaces: from atoms to complexity (Nobel lecture), *Angew. Chem. Int. Ed.* 47 (2008) 3524–3535.
- [4] K. Honkala, A. Hellman, I.N. Remediakis, A. Logadottir, A. Carlsson, S. Dahl, C.H. Christensen, J.K. Nørskov, Ammonia synthesis from first-principles calculations, *Science* 307 (2005) 555–558.
- [5] P. Wang, F. Chang, W. Gao, J. Guo, G. Wu, T. He, P. Chen, Breaking scaling relations to achieve low-temperature ammonia synthesis through LiH-mediated nitrogen transfer and hydrogenation, *Nat. Chem.* 9 (2017) 64–70.
- [6] S. Linic, P. Christopher, D.B. Ingram, Plasmonic-metal nanostructures for efficient conversion of solar to chemical energy, *Nat. Mater.* 10 (2011) 911–921.
- [7] J.M. Sanz, D. Ortiz, R. Alcaraz de la Osa, J.M. Saiz, F. González, A.S. Brown, M. Losurdo, H.O. Everitt, F. Moreno, UV plasmonic behavior of various metal nanoparticles in the near-and far-field regimes: geometry and substrate effects, *J. Phys. Chem. C* 117 (2013) 19606–19615.
- [8] X. Meng, T. Wang, L. Liu, S. Ouyang, P. Li, H. Hu, T. Kako, H. Iwai, A. Tanaka, J. Ye, Photothermal conversion of CO_2 into CH_4 with H_2 over group VIII nanocatalysts: an alternative approach for solar fuel production, *Angew. Chem. Int. Ed.* 126 (2014) 11478–11482.
- [9] K.I. Aika, K. Tamari, Ammonia catalysis and manufacture, in: A. Nielsen (Ed.), *Ammonia Synthesis over Non-Iron Catalysts and Related Phenomena*, Springer, Heidelberg, 1995, pp. 103–142.
- [10] Z.W. Seh, S. Liu, M. Low, S.Y. Zhang, Z. Liu, A. Mlayah, M.Y. Han, Janus Au-TiO₂ photocatalysts with strong localization of plasmonic near-fields for efficient visible-light hydrogen generation, *Adv. Mater.* 24 (2012) 2310–2314.
- [11] H. Yin, Y. Kuwahara, K. Mori, H. Cheng, M. Wen, Y. Huo, H. Yamashita, Localized surface plasmon resonances in plasmonic molybdenum tungsten oxide hybrid for visible-light-enhanced catalytic reaction, *J. Phys. Chem. C* 121 (2017) 23531–23540, <http://dx.doi.org/10.1021/acs.jpcc.7b08403>.
- [12] H. Yin, Y. Kuwahara, K. Mori, H. Cheng, M. Wen, H. Yamashita, High-surface-area plasmonic MoO_{3-x} : rational synthesis and enhanced ammonia borane dehydrogenation activity, *J. Mater. Chem. A* 5 (2017) 8946–8953.
- [13] E. Prodan, C. Radloff, N.J. Halas, P. Nordlander, A hybridization model for the plasmon response of complex nanostructures, *Science* 302 (2003) 419–422.
- [14] X. Chen, L. Liu, F. Huang, Black titanium dioxide (TiO_2) nanomaterials, *Chem. Soc. Rev.* 44 (2015) 1861–1885.
- [15] M. Kitano, Y. Inoue, Y. Yamazaki, F. Hayashi, S. Kanbara, S. Matsuishi, T. Yokoyama, S. Kim, M. Hara, H. Hosono, Ammonia synthesis using a stable electrode as an electron donor and reversible hydrogen store, *Nat. Chem.* 4 (2012) 934–940.
- [16] H. Tan, Z. Zhao, M. Niu, C. Mao, D. Cao, D. Cheng, P. Feng, Z. Sun, A facile and versatile method for preparation of colored TiO_2 with enhanced solar-driven photocatalytic activity, *Nanoscale* 6 (2014) 10216–10223.
- [17] F. Rosowski, A. Hornung, O. Hinrichsen, D. Herein, M. Muhler, G. Ertl, Ruthenium catalysts for ammonia synthesis at high pressures: preparation characterization, and power-law kinetics, *Appl. Catal. A-Gen.* 151 (1997) 443–460.
- [18] D. Ricci, C. Di Valentin, G. Pacchioni, P.V. Sushko, A.L. Shluger, E. Giannello, Paramagnetic defect centers at the MgO surface. An alternative model to oxygen vacancies, *J. Am. Chem. Soc.* 125 (2003) 738–747.
- [19] A. Ishikawa, T. Takata, J.N. Kondo, M. Hara, H. Kobayashi, K. Domen, Oxsulfide $\text{Sm}_2\text{Ti}_2\text{S}_2\text{O}_5$ as a stable photocatalyst for water oxidation and reduction under visible light irradiation ($\lambda \leq 650$ nm), *J. Am. Chem. Soc.* 124 (2002) 13547–13553.
- [20] Y. Xu, M.A. Schoonen, The absolute energy positions of conduction and valence bands of selected semiconducting minerals, *Am. Miner.* 85 (2000) 543–556.
- [21] S. Trasatti, The absolute electrode potential: an explanatory note (Recommendations 1986), *Pure Appl. Chem.* 58 (1986) 955–966.
- [22] M.W. Ribarsky, E.D. Palik (Ed.), *Handbook of Optical Constants of Solids I*, Academic Press, New York, 1985, pp. 799–804.
- [23] D.W. Lynch, W.R. Hunter, E.D. Palik (Ed.), *Handbook of Optical Constants of Solids III*, Academic Press, New York, 1998, pp. 256–261.
- [24] A. Naldoni, M. Allietta, S. Santangelo, M. Marelli, F. Fabbri, S. Cappelli, C.L. Bianchi, R. Psaro, V.D. Santo, Effect of nature and location of defects on bandgap narrowing in black TiO_2 nanoparticles, *J. Am. Chem. Soc.* 134 (2012) 7600–7603.
- [25] M.H. Rittmann-Frank, C.J. Milne, J. Rittmann, M. Reinhard, T.J. Penfold, M. Chergui, Mapping of the photoinduced electron traps in TiO_2 by picosecond X-ray absorption spectroscopy, *Angew. Chem. Int. Ed.* 53 (2014) 5858–5862.
- [26] L.X. Chen, T. Rajh, Z. Wang, M.C. Thurnauer, XAFS studies of surface structures of TiO_2 nanoparticles and photocatalytic reduction of metal ions, *J. Phys. Chem. B* 101 (1997) 10688–10697.
- [27] J.B. Priebe, M. Karnahl, H. Junge, M. Beller, D. Hollmann, A. Brückner, Water reduction with visible light: synergy between optical transitions and electron transfer in $\text{Au}-\text{TiO}_2$ catalysts visualized by in situ EPR spectroscopy, *Angew. Chem. Int. Ed.* 52 (2013) 11420–11424.
- [28] J.N. Schrauben, R. Hayoun, C.N. Valdez, M. Braten, L. Fridley, J.M. Mayer, Titanium and zinc oxide nanoparticles are proton-coupled electron transfer agents, *Science* 336 (2012) 1298–1301.
- [29] X. Chen, L. Liu, Z. Liu, M.A. Marcus, W.C. Wang, N.A. Oyler, M.E. Grass, B. Mao, P.A. Glans, P.Y. Yu, J. Guo, S.S. Mao, Properties of disorder-engineered black titanium dioxide nanoparticles through hydrogenation, *Sci. Rep.* 3 (2013) 1510.
- [30] N. Liu, C. Schneider, D. Freitag, M. Hartmann, U. Venkatesan, J. Müller, S. Erdmann, P. Schmuki, Black TiO_2 nanotubes: cocatalyst-free open-circuit hydrogen generation, *Nano Lett.* 14 (2014) 3309–3313.
- [31] P. Martelli, R. Caputo, A. Remhof, P. Mauron, A. Borgschulte, A. Züttel, Stability and decomposition of NaBH_4 , *J. Phys. Chem. C* 114 (2010) 7173–7177.
- [32] X. Chen, L. Liu, Y.Y. Peter, S.S. Mao, Increasing solar absorption for photocatalysis with black hydrogenated titanium dioxide nanocrystals, *Science* 331 (2011) 746–750.
- [33] Z. Wang, C. Yang, T. Lin, H. Yin, P. Chen, D. Wan, F. Xu, F. Huang, J. Lin, X. Xie, M. Jiang, H-doped black titania with very high solar absorption and excellent photocatalysis enhanced by localized surface plasmon resonance, *Adv. Funct. Mater.* 23 (2013) 5444–5450.
- [34] G. Xi, J. Ye, Q. Ma, N. Su, H. Bai, C. Wang, In situ growth of metal particles on 3D urchin-like WO_3 nanostructures, *J. Am. Chem. Soc.* 134 (2012) 6508–6511.
- [35] L. Di, N. Ichikuni, S. Shimazu, T. Uematsu, Hydrogenation of CO_2 over sprayed Ru/TiO_2 fine particles and strong metal-support interaction, *Appl. Catal. A-Gen.* 180 (1999) 227–235.
- [36] W. Zhan, Q. He, X. Liu, Y. Guo, Y. Wang, L. Wang, Y. Guo, A.Y. Borisevich, J. Zhang, G. Lu, S. Dai, A sacrificial coating strategy toward enhancement of metal-support interaction for ultrastable Au nanocatalysts, *J. Am. Chem. Soc.* 138 (2016) 16130–16139.
- [37] K.I. Aika, Role of alkali promoter in ammonia synthesis over ruthenium catalysts—Effect on reaction mechanism, *Catal. Today* 286 (2017) 14–20.
- [38] S. Sayan, M. Kantcheva, S. Suzer, D.O. Uner, FTIR characterization of Ru/SiO_2 catalyst for ammonia synthesis, *J. Mol. Struct.* 480 (1999) 241–245.
- [39] P. Avenier, M. Taoufik, A. Lesage, X. Solans-Monfort, A. Baudouin, A. De Mallmann, L. Veyre, J.-M. Basset, O. Eisenstein, L. Emsley, E.A. Quadrelli, Dinitrogen dissociation on an isolated surface tantalum atom, *Science* 317 (2007) 1056–1060.
- [40] H. Hirakawa, M. Hashimoto, Y. Shiraishi, T. Hirai, Photocatalytic conversion of nitrogen to ammonia with water on surface oxygen vacancies of titanium dioxide, *J. Am. Chem. Soc.* 2017 (139) (2017) 10929–10936.
- [41] M. Kitano, Y. Inoue, H. Ishikawa, K. Yamagata, T. Nakao, T. Tada, S. Matsuishi, T. Yokoyama, M. Hara, H. Hosono, Essential role of hydride ion in ruthenium-based ammonia synthesis catalysts, *Chem. Sci.* 7 (2016) 4036–4043.
- [42] M. Hara, M. Kitano, H. Hosono, Ru-loaded C12A7: e^- electrode as a catalyst for ammonia synthesis, *ACS Catal.* 7 (2017) 2313–2324.
- [43] W. Gao, P. Wang, J. Guo, F. Chang, T. He, Q. Wang, G. Wu, P. Chen, Barium hydride-mediated nitrogen transfer and hydrogenation for ammonia synthesis: a case study of cobalt, *ACS Catal.* 7 (2017) 3654–3661.
- [44] P. Wang, H. Xie, J. Guo, Z. Zhao, X. Kong, W. Gao, F. Chang, T. He, G. Wu, M. Chen, L. Jiang, P. Chen, The formation of surface lithium-iron ternary hydride and its function on catalytic ammonia synthesis at low temperatures, *Angew. Chem. Int. Ed.* 56 (2017) 1–6.
- [45] W. Raróg-Pilecka, E. Miśkiewicz, D. Szmigiel, Z. Kowalczyk, Structure sensitivity of ammonia synthesis over promoted ruthenium catalysts supported on graphitized carbon, *J. Catal.* 231 (2005) 11–19.
- [46] M. Pelton, G.W. Bryant, *Introduction to metal-nanoparticle plasmonics*, Wiley-ScienceWise, Hoboken, 2013, pp. 39–46.